


**Meissner hole in pristine and proton-irradiated  $\text{Ba}_{1-x}\text{Rb}_x\text{Fe}_2\text{As}_2$** Tong Ren , Sunseng Pyon, and Tsuyoshi Tamegai*Department of Applied Physics, The University of Tokyo, 7-3-1 Hongo, Bunkyo-ku, Tokyo 113-8656, Japan*

(Received 6 March 2024; revised 22 April 2024; accepted 17 May 2024; published 5 June 2024)

We investigated the unstable interface between vortices and antivortices in single crystals of the iron-based superconductor  $(\text{Ba}_{0.67}\text{Rb}_{0.33})\text{Fe}_2\text{As}_2$  ( $T_c \sim 37.6$  K). This interface, also known as the Meissner hole, was captured with magneto-optical imaging in both a pristine crystal and one with artificial point defects. We confirmed the presence of local excess current flowing along the interface. The dynamics of such an interface qualitatively follows the prediction of the critical state model, accompanied by a finite relaxation rate of magnetization. However, quantitatively, the local relaxation of the Meissner hole can be much faster than that of magnetization due to local deformation of the excess current.

DOI: [10.1103/PhysRevB.109.224504](https://doi.org/10.1103/PhysRevB.109.224504)**I. INTRODUCTION**

When the applied field is reduced to zero from a sufficiently large value in superconductors with a small demagnetization factor (thin slab with parallel field), a full critical state is formed. In this state, there flows a unidirectional current that amounts to the critical value. A further reduction of the applied field toward negative values, called remagnetization, simply introduces antivortices with a well-defined boundary between pre-existing vortices. However, the situation becomes complicated in superconductors with a demagnetization factor close to unity (thin sample with perpendicular field). Near the boundary separating two regions with opposite polarities of vortices, vortices naturally form closed loops due to the presence of a large in-plane component of the field. Such vortex loops have minimum diameters surrounding the vortex-free region, called a Meissner hole (or referred to as “current strings” in some cases [1,2]). Experiments by Vlasko-Vlasov showed the presence of such cylindrical structures in  $\text{YBa}_2\text{Cu}_3\text{O}_7$  [3]. The most intriguing feature in the magneto-optical images of the Meissner hole is its unique meandering boundary. Such behavior of vortices can be considered as macroturbulence and is usually described as a consequence of instability at the vortex-antivortex interface [4–7]. Since its discovery, a few attempts have been made to interpret this phenomenon, yet the discussion is still open. The instability was initially attributed to the heat released by vortex-antivortex annihilation [7,8]. A more plausible argument drew an analogy between the planar front of vortices with the fluid surface and claimed that simple hydrodynamics is sufficient to explain the instability [4]. In this theory, an in-plane velocity shear of vortices and antivortices induced by the *ab*-plane lattice anisotropy (a.k.a., the twin boundary) triggers the well-known Kelvin-Helmholtz instability in usual fluid mechanics [9]. However, as is pointed out by Ref. [6], the anisotropy required for this scenario is too large for any known realistic system. Even if such a system ever exists, the interface can still be stabilized in a dynamic model where the vortex front is propagating toward the interior of the superconductor, known as the relaxation of magnetization.

As an extension to existing theories and experiments, much of this paper has taken the relaxation of vortices into consideration. We decided to study the effect of the Meissner hole on low-field (at fields that are close to or smaller than the self-field) vortex dynamics, particularly focusing on magnetic relaxation. Besides, according to the model proposed in Refs. [3,10,11], at the skin layer of the Meissner hole, there flows a local excess current which is twice as large as the critical current in the same area. The role such a current plays in the low-field vortex state is another issue to be investigated.

In this work, we obtain high-resolution images of Meissner holes by employing magneto-optical (MO) imaging in 122-type iron-based superconductor (IBS)  $(\text{Ba}_{0.67}\text{Rb}_{0.33})\text{Fe}_2\text{As}_2$  single crystals. This is another material in which the Meissner hole is confirmed experimentally after  $\text{YBa}_2\text{Cu}_3\text{O}_7$  [3–5,12–15],  $\text{MgB}_2$  [16], and  $\text{Ba}(\text{Fe}_{1-x}\text{Co}_x)_2\text{As}_2$  [17]. Our analysis is aimed at the vortex dynamics at the low-field state of a remagnetized superconductor. We modeled the motion of the Meissner hole using the theory of magnetic relaxation. Then, we track the Meissner hole for over an hour and analyze its mobility by referring to the relaxation of magnetization of the same material. At the end of the article, we discuss how the anisotropy of superconductivity influences the formation of vortex loops.

**II. EXPERIMENTAL METHODS**

Single crystals of  $(\text{Ba}_{1-x}\text{Rb}_x)\text{Fe}_2\text{As}_2$  were synthesized by a FeAs self-flux method similar to that used for  $(\text{Ba}_{1-x}\text{Na}_x)\text{Fe}_2\text{As}_2$  [18] and  $(\text{Ba}_{1-x}\text{K}_x)\text{Fe}_2\text{As}_2$  [19]. Presynthesized BaAs, RbAs, FeAs, and  $\text{FeAs}_2$  powders were used as starting ingredients. FeAs was prepared by sealing stoichiometric amounts of Fe powder (99.9%, Koujundo Chemical Laboratory) and As grains (7N, Hurukawa Denshi) in an evacuated quartz tube followed by slow heating up to 700 °C for 2 days. A similar sequence was used in preparing  $\text{FeAs}_2$  with the highest temperature of 750 °C. BaAs and RbAs were synthesized from Ba pieces (99.9%, Furuuchi Chemical) and Rb (99.6%, Sigma-Aldrich) ingot mixed with As grains at temperatures of 650 and 170 °C, respectively. To obtain

$(\text{Ba}_{1-x}\text{Rb}_x)\text{Fe}_2\text{As}_2$  crystals, a mixture with a ratio of BaAs : RbAs : FeAs :  $\text{FeAs}_2 = 1 - x : 1.3x : 2 : 1$  of 3.5 g in total was loaded into an alumina crucible and then further sealed inside a stainless steel tube under inert atmosphere. All these operations were done in a glove box filled with an argon atmosphere. The capped stainless steel tube was heated up firstly to 600 °C for 5 h, then to 1100 °C, held for half a day, followed by cooling to 800 °C at 5 °C/h. Crystals grown with this method have mirrorlike surfaces with typical dimensions of  $\sim 1 \times 1 \times 0.05 \text{ mm}^3$ . To study the Meissner hole in a crystal with a controlled amount of disorder, 3-MeV proton irradiations were performed using the Heavy Ion Medical Accelerator (HIMAC) at the National Institute of Radiological Sciences. For certain purposes, some of these crystals were partly masked with a 200- $\mu\text{m}$ -thick gold foil before irradiation to block direct proton beam. The setup of one of such crystals can be found in the Supplemental Material [20].

The magnetization of the pristine and irradiated crystals was tracked using a superconducting quantum interference device (SQUID) magnetometer (MPMS-5XL, Quantum Design). The relaxation of the magnetization in a single crystal under its critical state is discussed using Anderson's model [21], where the normalized relaxation rate  $S$  is defined as

$$S \equiv \left| \frac{d \ln M}{d \ln t} \right|. \quad (1)$$

For the investigation of the Meissner hole, the distribution of the magnetic induction at the crystal surface was captured by differential MO imaging, where integrated backgrounds were subtracted from the integrated target image [22,23]. By doing so, it is possible to obtain high-resolution MO images with suppressed fluctuations caused by the environments. After being exposed over 0.1 s and integrated 10 times, the induction resolution of the image easily reaches  $\sim 0.1 \text{ G}$  as is shown in our previous publications [24]. It is noteworthy that our MO setup is only capable of resolving the vertical components of flux densities integrated along the indicator film outside the sample. In some situations, this may deviate from the realistic  $B$  controlling the vortex pinning inside the sample.

### III. RESULTS AND DISCUSSION

#### A. Relaxation of magnetization in single crystals

Since our interest lies in relating the vortex dynamics in superconductors, especially at low fields, to the formation and dynamics of the Meissner hole, we initially traced the bulk magnetization of both pristine and proton-irradiated single crystals at various temperatures and fields. Figure 1 shows the field dependence of the normalized relaxation rate of magnetization in both pristine and proton-irradiated crystals. Here  $t$  is the elapsed time after the critical state is created. The global magnetic-field dependence of the normalized relaxation rate  $S(H)$  shown in Fig. 1(a) is explained in the framework of the weak collective creep theory using a glassy exponent  $\mu$  [25–27]. The theory predicted the relation rate  $S \propto \mu^{-1}$ .  $S(H)$  shows a characteristic increase towards low fields when vortices creep individually and  $\mu$  takes a small value of  $1/7$ . It becomes field independent at larger fields where vortices creep in small bundles with  $\mu = 5/2$ . That said, in many experimental situations including the present

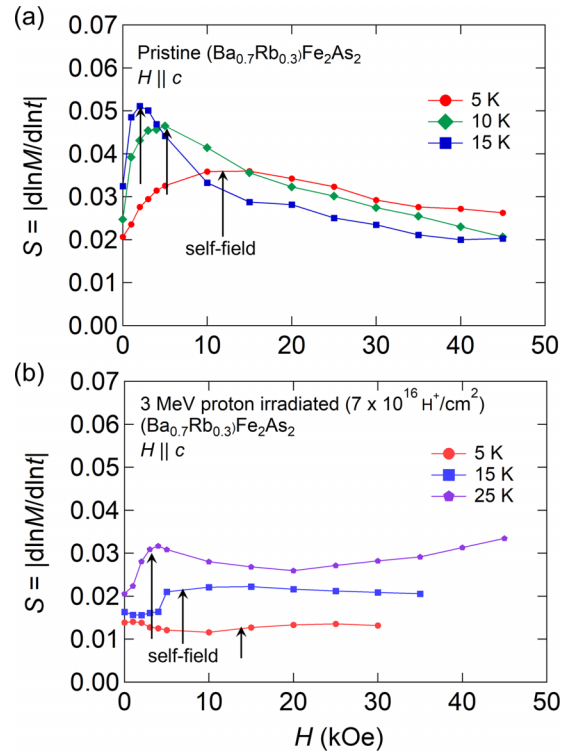


FIG. 1. Magnetic field dependence of the normalized relaxation rate of magnetization  $S(H)$  in (a) a pristine crystal and (b) a crystal irradiated with 3-MeV protons to a dose of  $7 \times 10^{16} \text{ H}^+/\text{cm}^2$ . The black arrows mark the location of the self-field.

one, the ideal single-vortex creep regime is never achieved due to the presence of sparse strong-pinning centers that pre-exist in the pristine crystal. This suppressed the peak corresponding to  $\mu = 1/7$  at low fields. The maximum value of  $S$  at low fields in the pristine crystal increases as pinning becomes weaker at higher temperatures, leading to a smaller field distribution in the sample. The strong suppression of  $S(H)$  at fields below the self-field of the sample (marked by black arrows) is still under debate. Here the self-field is approximated by  $H_{\text{sf}} \sim J_c d$ , where  $J_c$  is the critical current density and  $d$  is the thickness of the sample. In some cases, such suppression is attributed to the appearance of the Meissner hole [28].

After introducing point defects via 3-MeV proton irradiation, the extra-strong-pinning centers drastically enhance the pinning force [27,29], causing considerable variation in the behavior of  $S$ . The low-field peak is almost entirely suppressed due to the introduction of strong-pinning centers, as shown in Fig. 1(b). However, the suppression of  $S(H)$  at fields lower than the self-field is still observable at 5 and 15 K. These behaviors of  $S$  in pristine and proton-irradiated  $(\text{Ba}_{0.67}\text{Rb}_{0.33})\text{Fe}_2\text{As}_2$  are very similar to those reported for  $(\text{Ba}_{0.6}\text{K}_{0.4})\text{Fe}_2\text{As}_2$  [19] and  $\text{Ba}(\text{Fe}_{0.93}\text{Co}_{0.07})_2\text{As}_2$  [30].

#### B. Meissner hole in pristine crystal

To distinguish the initial magnetization from the remagnetized state, which is our primary focus, we start by observing the virgin penetration process in a pristine crystal. The crystal was first cooled to 15 K without field. Then an external field

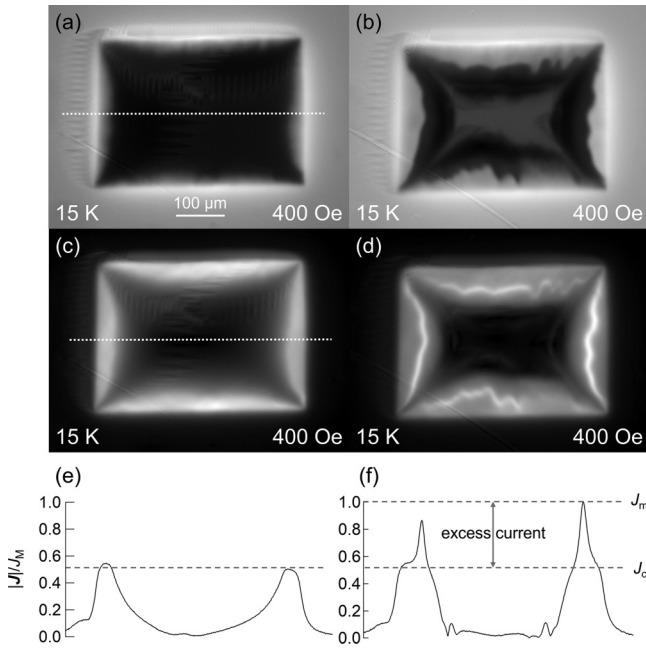


FIG. 2. MO images of crystals after (a) virgin penetration and (b) the remagnetization process. The analyzer is adjusted to display the magnetic field proportionally to the light intensity so that vortices are the bright region and antivortices are the dark region. Panels (c) and (d) are mappings of the in-plane current density  $|\mathbf{J}|$  converted from  $B$  mappings in panels (a) and (b), respectively, using inverse Biot-Savart law.  $|\mathbf{J}|$  profiles normalized by  $J_{\max}$  along the dotted line in panels (c) and (d) are shown in panels (e) and (f), respectively.

was increased up to 600 Oe at a step of 100 Oe. Figure 2(a) shows the MO image of the crystal being penetrated from the perfect Meissner state. Weakly irregular penetration of vortices from some edges probably originates from the inhomogeneous distribution of pinning centers and/or minute defects at the crystal edge. The induction drops smoothly from the edge of the crystal as shown in Fig. 3(a), showing the induction profile along the white dotted line in Fig. 2(a).

The remagnetization process in the same crystal is then followed. The magnetization process is almost identical to that for the virgin penetration, except that the crystal was initially premagnetized by a negative field of  $-1000$  Oe before the positive field was applied. Figure 2(b) shows the crystal being remagnetized by the same positive field as that applied in Fig. 2(a). The remagnetization front between vortices and antivortices appears as the boundary between the bright and dark regions. The front shows distinct behavior compared with that in virgin penetration. The vortex-antivortex interface is extremely curled and tends to penetrate deeper into the sample than the virgin case. The remagnetization front progresses towards the interior of the crystal as the field increases while maintaining almost the same pattern, generating the  $B_z(x)$  profile displayed in Fig. 3(b), which is taken from Fig. 2(b) along the same dotted line in Fig. 2(a). Unlike the virgin situation, sharp drops of magnetic induction (marked by black arrows) are spotted at the remagnetization front where  $B_z = 0$ . This local magnetic field distortion is supposed to be induced by the integrated Meissner current, which is twice as large as the integrated  $J_c$ . We then further extend the observation to

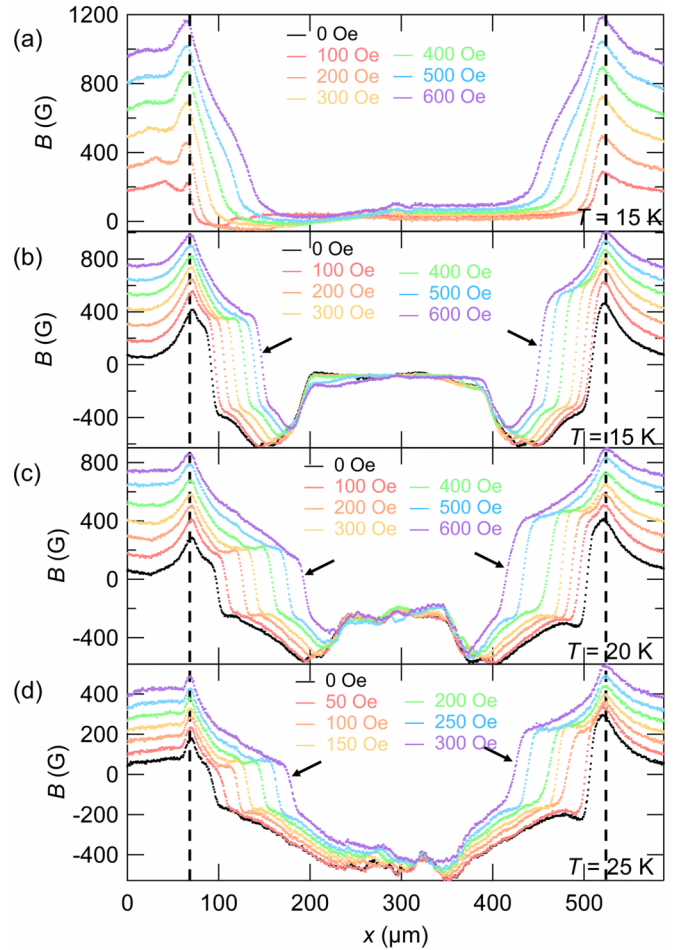


FIG. 3.  $B_z(x)$  profiles taken along the white dotted line in Figs. 2(a) and 2(b): (a) virgin penetration case and (b)–(d) remagnetized cases at different temperatures. The dashed lines indicate the edges of the crystal, and the black arrows mark the induction steps induced by the local excess current.

higher temperatures [see Figs. 3(c) and 3(d)]. The meandering visually persists close to  $T_c$ , while the induction steps are not well-resolved at temperatures above  $\sim 30$  K.

Since the evidence provided by the  $B_z$  profile points directly to the existence of a local excess current, we convert the  $B_z$  map into a  $|\mathbf{J}|$  map using inverse Biot-Savart's law [17]. Here, we assume that the induction is caused by a two-dimensional sheet current. It is worth noting that this assumption does not accurately reflect the realistic scenario, as the Meissner hole is consistently accompanied by out-of-plane current flows, especially at the top and bottom regions of the vortex loop. However, these currents are mostly canceled out by neighboring vortices since they have opposite out-of-plane current components, and any modulation will be too subtle for MO to capture. The in-plane current densities are mapped in Fig. 2(d). As a reference, the  $|\mathbf{J}|$  distribution in virgin penetration is also shown in Fig. 2(c). The brightness in the graph represents the strength of the in-plane current density. Like the shape of the remagnetization front, the conducting path of the excess current in Fig. 2(d) is curvy and mostly continuous, while the current flows uniformly in



Fig. 2(c). Figures 2(e) and 2(f) are corresponding normalized  $|J|$  profiles along the dotted lines in Figs. 2(c) and 2(d), respectively. The graphs are normalized by the maximum value in the profile, namely  $J_{\max}$ . In the remagnetized state, a spikelike structure is spotted at the tip of the peak in the profile. On the other hand, in the profile of virgin penetration, no significant structure is found at the same location. It should be noted that the magnitude of  $J_c$  in the remagnetized sample, which corresponds to the plateau value close to the sample edge, is roughly half of  $J_{\max}$ . Thus, we can safely conclude that, in the low-field remagnetized state of the pristine  $(\text{Ba}_{0.67}\text{Rb}_{0.33})\text{Fe}_2\text{As}_2$ , there exists an unstable interface between vortices and antivortices associated with the Meissner hole. Within the skin layer of the Meissner hole, a doubled current is flowing. In some theory, such excess current could intensify the interfacial instability [31].

### C. Dynamics of the Meissner hole

The remagnetization process including vortex dynamics in a type-II superconductor is usually discussed using a one-dimensional critical state model [32,33]. We applied the same model to the motion of the Meissner hole, as shown below. Here, we ignore the contribution of the Meissner current flowing on the surface of the sample. Consider a platelike superconducting single crystal with thickness  $h$  and width  $2d$  ( $d \gg h$ ) in the critical state. The perpendicular component of the magnetic field  $B_{z0}(x)$  on the sample plane induced by the critical current density  $J_c$  is given by

$$B_{z0}(x) = -\frac{2J_c h}{c} \ln \left| \frac{d^2 - x^2}{x^2} \right|, \quad (2)$$

where  $x = 0$  is the center of the sample and  $c = 10$  is the speed of light in Gaussian units with keeping the unit of  $J_c$  to A/cm<sup>2</sup>. Here we approximated a sheet-thin current. Under a finite external field  $H_{\text{ext}}$ , the location of the Meissner hole  $x_M$  defined by  $B_{z0}(x_M) + H_{\text{ext}} = 0$  is expressed as

$$x_M = \pm \frac{d}{\sqrt{e^\alpha + 1}}, \quad \alpha = \frac{cH_{\text{ext}}}{2J_c h}. \quad (3)$$

On the other hand, according to Anderson's model,  $J_c$  is relaxing logarithmically with time [21,34]. Such relaxation in  $J_c$  causes the Meissner hole to move toward the center (the edge) of the crystal for  $H_{\text{ext}} > 0$  ( $H_{\text{ext}} < 0$ ). By defining a normalized creep rate of the Meissner hole,  $S_{\text{MH}} = |x_M^{-1} dx_M / d \ln t|$ , one finds that it is related to the normalized relaxation of the magnetization  $S$  as follows,

$$\begin{aligned} S_{\text{MH}} &= \frac{d \ln x_M}{d \ln t} \\ &= -\frac{1}{2} \left( \frac{e^\alpha}{e^\alpha + 1} \right) \frac{d\alpha}{d \ln J_c} \frac{d \ln J_c}{d \ln t} \\ &= \frac{\alpha}{2} \frac{e^\alpha}{e^\alpha + 1} S \\ &= \beta S, \end{aligned} \quad (4)$$

where

$$\beta = \frac{\alpha}{2} \frac{e^\alpha}{e^\alpha + 1}. \quad (5)$$

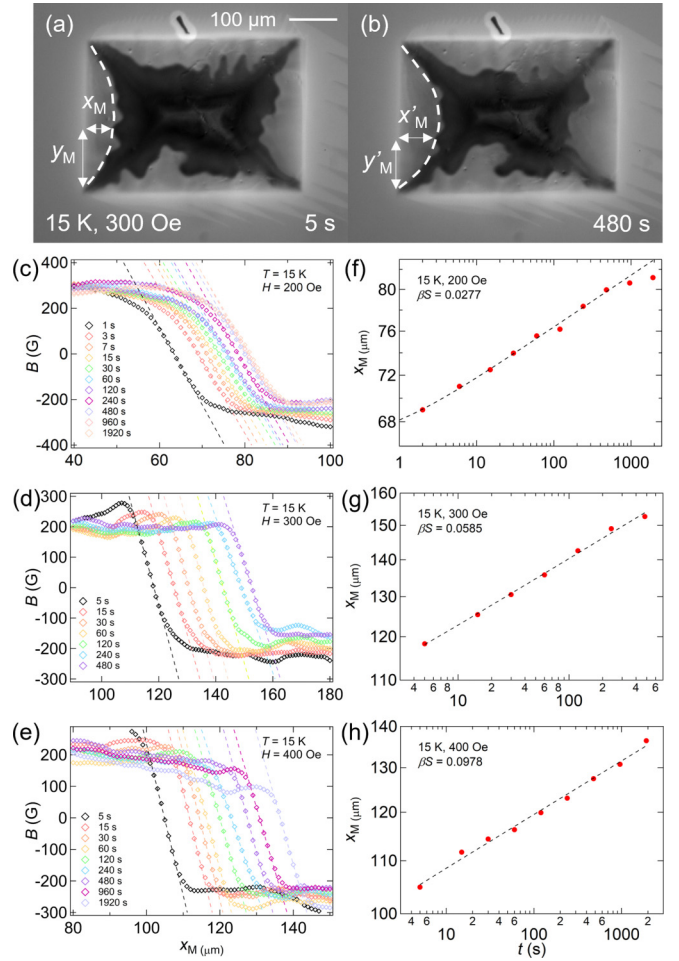


FIG. 4. Magneto-optical images of Meissner holes in a  $(\text{Ba}_{0.67}\text{Rb}_{0.33})\text{Fe}_2\text{As}_2$  single crystal (a) 5 s and (b) 480 s after the remagnetization. The remagnetization is done by zero-field cooling to 15 K, followed by initial magnetization with  $-1000$  Oe and remagnetization with 300 Oe. White dashed lines are fictitious boundaries representing average penetration of the external field. Time evolution of the induction profiles along the horizontal double-headed arrow in panel (a) at 15 K and at (c) 200 Oe, (d) 300 Oe, and (e) 400 Oe. The location of the Meissner hole,  $x_M$ , as a function of time at (f) 200 Oe, (g) 300 Oe, and (h) 400 Oe. The plots are in logarithmic scale, and the black dashed lines are fittings to Eq. (4).

In this way,  $\beta$ , which is a parameter that depends on the external field, and  $J_c$  serve as a measure of the mobility of the Meissner hole. This parameter could be extracted by evaluating the creep rate of the Meissner hole, as far as  $S$  is known. Later, the  $\beta S$  obtained in such a manner is compared to  $S$  directly measured with a SQUID magnetometer to verify this simple model.

The motion of the Meissner hole of an optimally doped crystal is tracked over half an hour. The Meissner hole in such a crystal shown in Fig. 4(a) is created by zero-field cooling to 15 K, followed by a virgin penetration with  $-1000$  Oe and remagnetization with 300 Oe. The Meissner hole relaxes into Fig. 4(b) after 480 s after the remagnetization. The methodology for tracking a certain segment of the Meissner hole is described below. We first pick a local minimum/maximum

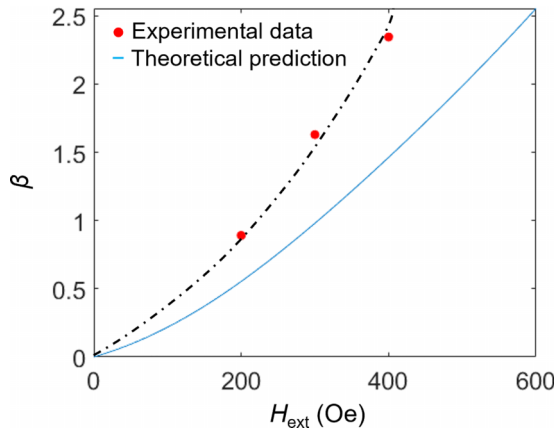


FIG. 5. Experimentally determined magnetic-field dependence of  $\beta$ , which is evaluated by dividing  $\beta S$  obtained from the fitting in Figs. 4(f), 4(g), and 4(h) by  $S$  in Fig. 1(a). The blue solid line is a theoretical prediction of  $\beta$  defined in Eq. (5), which is calculated with a field-dependent  $J_c$  at 15 K (see Supplemental Material [20]) and  $h = 10 \mu\text{m}$  for the sample shown in Fig. 4.

of the wavy boundary located on a fictitious boundary [white dashed line in Fig. 4(a), which represents the average penetration depth of the boundary]. Since the remagnetized boundary maintains an approximate geometry during propagation, we could guide the trajectory of this local maximum/minimum [ $x_M(t)$ ,  $y_M(t)$ ] to the eye during its relaxation, and the horizontal motion  $x_M(t)$  of the segment should follow the prediction of Eq. (4). Figures 4(c)–4(e) show the time evolution of the induction profiles at three different external fields along the horizontal double-headed arrow in Figs. 4(a) and 4(b). With the knowledge that the Meissner hole is a vortex-free region where  $B_z = 0$ , one can easily determine its location as a function of time as shown in Figs. 4(f)–4(h). Fitting the data points with Eq. (4) yields the normalized creep rate of the Meissner hole  $S_{\text{MH}} = \beta S$ . By comparing it with the normalized relaxation of magnetization  $S$  in Fig. 1(a), we can evaluate the external field dependence of  $\beta$ , as shown in Fig. 5. The experimental data (red points) show a field dependence similar to the prediction by Eq. (5) (blue line). However, the creep rate of the Meissner hole is considerably larger than the calculation, indicating that the vortices and antivortices at the remagnetization boundary form a rather unstable structure so that the equilibrium could be easily broken by a tiny change in the external field (200 Oe) compared to the stronger self-field of the single crystal ( $\sim 800$  Oe). When the external field is close to zero,  $\beta$  seems to be convergent. At finite external fields, the real motion of the Meissner hole is faster than the theoretical prediction (blue line) by roughly 60%. Such quantitative discrepancy agrees with the fact that the remagnetization boundary propagates conspicuously deeper into the bulk than the virgin penetration boundary in Fig. 2. It may be required to include another feature of the Meissner hole to explain this acceleration, the curly nature of the remagnetization boundary. Since the Meissner hole is inherently curly and meandering, the current segments around a swerve are dragged by the Lorentz force due to the magnetic fields induced by each other, as sketched in Fig. 6. Such interaction could mechanically accelerate the annihilation of vortices and

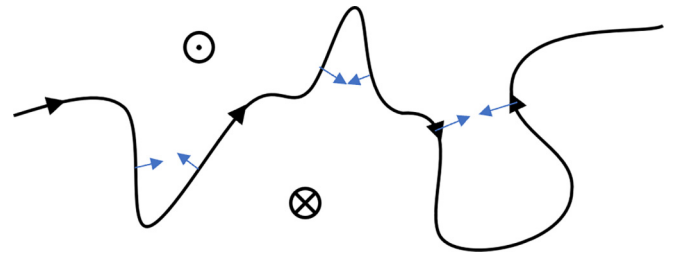


FIG. 6. Schematics of the meandering remagnetized boundary between vortices and antivortices. Black arrows indicate the direction of the Meissner current. Blue smaller arrows stand for the Lorentz force exerted on certain current segments.

antivortices at the boundary by pulling them closer. Figure 7 shows a typical scene of such a situation. In this special sample, we magnified the inhomogeneity by irradiating the right rectangular area with 3-MeV protons. The Meissner hole appearing as a black wiggling ring is created after field-cooling the crystal at  $-1000$  Oe, followed by the application of an 800-Oe field. Since the irradiated region contains extra defects created by high-energy protons, the Meissner hole is strongly bent due to the inability of flux to penetrate this domain where a much larger screening current is flowing [19,28,35]. As a consequence, a dramatic curvature is found near the border of the pristine and irradiated regions, marked by the upper white arrow in Fig. 7(a). This portion of the strongly curved boundary moves rapidly towards the sample center and finally collides with another coming from the top [Fig. 7(c)]. A large single loop of the Meissner hole is thereafter disconnected into two [Fig. 7(d)]. A similar situation is seen at the location marked by the lower white arrow in Fig. 7(a). Here, a mini

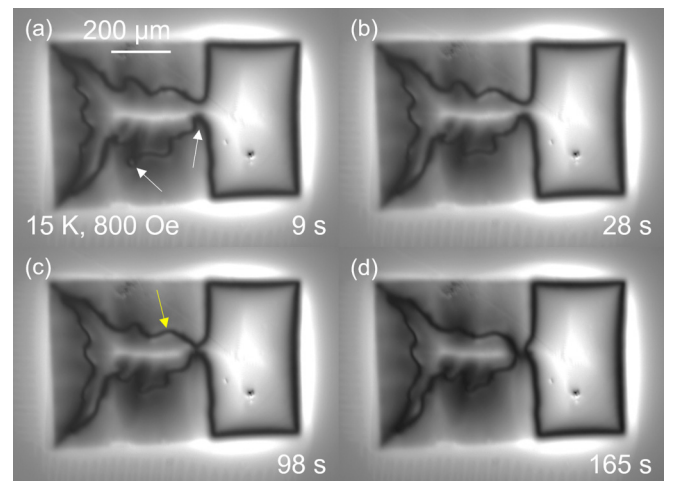


FIG. 7. Magneto-optical images of the Meissner hole in a partly irradiated crystal at (a) 9 s, (b) 28 s, (c) 98 s, and (d) 165 s after the completion of remagnetization. The crystal was field-cooled to 15 K at  $-1000$  Oe, followed by remagnetization with 800 Oe. The polarizer and the analyzer are adjusted perpendicular to each other so that the Meissner hole shows up as a black wiggling ring. The white arrows mark typical segments on the remagnetization boundary with phenomenal curvatures, while the yellow one indicates an opposite case.

loop of the Meissner hole splits from the main one due to a similar mechanism and annihilates itself within less than 20 s in Fig. 7(b). Such an active motion is a rare observation compared to other locations on the Meissner hole with milder curvatures, e.g., at the location marked by the yellow arrow in Fig. 7(c). As shown in Fig. 2(b), a curly and wiggling boundary is ubiquitous in the remagnetized crystal, while such a deformation of the boundary is not observed in the normally magnetized crystal. In addition, the remagnetization boundary, at least locally, always tends to penetrate deeper into the crystal, as shown in Figs. 3(a) and 3(b). This evidence may support the hypothesis that the motion of the Meissner hole is accelerated by the extra Lorentz force that comes with its geometry. However, the configurational factor described above makes the local motion of the Meissner hole less predictable, and the quantitative evaluation made in Fig. 5 might not be a comprehensive picture. On top of that, some segments of the Meissner hole did not follow the prediction of our model. Sometimes, they were static, leaping, or even retreating in the course of relaxation, and attempts to extract  $S_{MH}$  at such spots have led to failures in the  $x_{M-t}$  logarithmic fitting.

#### D. Meissner current

The equilibrium between flux tension and its pinning force determines the minimum radius of the Meissner hole,  $R_M = cH_{c1}/4\pi J_c$ , and any vortex loop smaller than this shall collapse on itself [3]. As for the crystal analyzed in Fig. 4,  $R_M$  is calculated as  $\sim 1 \mu\text{m}$  ( $H_{c1}(15 \text{ K}) \sim 100 \text{ G}$ ,  $J_c(15 \text{ K}, 300 \text{ G}) \sim 8 \times 10^5 \text{ A/cm}^2$ , see Supplemental Material [20]). Given the minimal radius, the extra current  $I_M - I_c = \pi R_M^2 J_c = 0.025 \text{ A}$  induces an  $\sim 5 \text{ G}$  maximum perpendicular magnetic field  $B_z$ ,  $5 \mu\text{m}$  above the center plane, which corresponds to the location where MO imaging is performed. However, the profiles in Figs. 4(c)–4(e) clearly exhibit an induction step of  $\sim 200 \text{ G}$  that is by an order of magnitude larger, assuming a compact (within  $1 \mu\text{m}$  separation) assembly of the garnet and the crystal. If the pinning-tension balance is strictly satisfied ( $I_M = 2\pi R_M^2 J_c$ ), in an isotropic model of superconductivity, this requires a  $\sim 7$  times larger radius of the Meissner hole, which by no means could exist since it simply exceeds the sample thickness of  $10 \mu\text{m}$ . Following the argument developed in Ref. [3] taking into account the anisotropy of superconductivity, we attempt to explain this discrepancy. We consider an isolated vortex segment pointing in a direction at an angle  $\theta$  with respect to the  $c$  axis. From Ref. [27], the line energy per unit length of a vortex segment is

$$e(\theta) = \varepsilon_0 \varepsilon(\theta) \ln \left( \frac{\kappa}{\varepsilon(\theta)} \right), \quad (6)$$

where

$$\varepsilon(\theta) = (\cos^2 \theta + \gamma^2 \sin^2 \theta)^{-1/2}, \quad (7)$$

where  $\gamma = \lambda_c/\lambda_{ab}$  is the angle-dependent anisotropy parameter,  $\varepsilon_0 = (\Phi_0/4\pi\lambda_{ab})^2 = (\Phi_0/4\pi)H_{c1}^c/\ln \kappa$ , and  $\kappa = \lambda/\xi \sim 100$  for  $(\text{Ba}_{0.6}\text{K}_{0.4})\text{Fe}_2\text{As}_2$  [36,37] is the Ginzburg-Landau parameter. The line tension is then given by [38]

$$\sigma = e(\theta) + \frac{d^2 e(\theta)}{d\theta^2}. \quad (8)$$

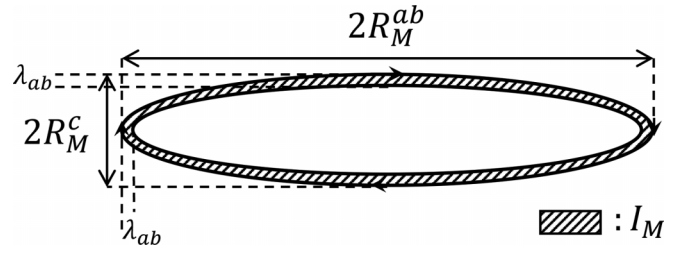


FIG. 8. Sketch of an elliptical Meissner hole of vertical and horizontal dimensions  $R_M^c \sim 0.4 \mu\text{m}$  and  $R_M^{ab} \sim 2 \mu\text{m}$ , respectively.  $\lambda \ll R_M$  is the penetrated skin depth where the Meissner current (hatched area) flows.

After some algebra, the following expressions for the line tension along both  $c$  and  $ab$  directions can be derived:

$$\sigma_c = \varepsilon_0 [1 + (\ln \kappa - 1)\gamma^{-2}], \quad (9)$$

$$\sigma_{ab} = \varepsilon_0 \gamma [\ln(\kappa \gamma) - 1 + \gamma^{-2}]. \quad (10)$$

With  $\gamma = \lambda_c/\lambda_{ab} \sim 2$  for  $(\text{Ba}_{0.55}\text{K}_{0.45})\text{Fe}_2\text{As}_2$  [39] (in Ref. [40]  $\gamma > 3$ ), when the balance between the line tension force  $F_l(\theta) = \sigma(\theta)/R_M(\theta)$  and the pinning force  $F_p(\theta) = J_c(\theta)\Phi_0/c$  is achieved, we obtain the radius for the elliptical Meissner hole  $R_M(\theta)$ . For  $\theta = 0^\circ$ , we obtain the radius for the Meissner hole along the  $c$  axis:  $R_M^c = 1.9\varepsilon_0/F_p = 0.41R_M$ . Unfortunately, the anisotropic pinning-force density in  $(\text{Ba}_{1-x}\text{Rb}_x)\text{Fe}_2\text{As}_2$  for fields parallel to the  $c$  axis ( $F_p^c$ ) and the  $ab$  plane ( $F_p^{ab}$ ) is not known. So, for simplicity we assume  $F_p^c = F_p^{ab} = F_p$ , which gives the radius for the Meissner hole along the  $ab$  plane:  $R_M^{ab} = 9.1\varepsilon_0/F_p = 1.98R_M$ . The schematic of such a Meissner hole is depicted in Fig. 8. The integrated Meissner current is estimated by approximating the elliptical Meissner hole into four segments: the upper and lower segments of total length  $\sim \pi R_M^{ab}$  with the Meissner current density per unit length  $J_M^{ab}\lambda_{ab} \sim cH_{c1}^{ab}/4\pi$ , and the side segments of total length  $\sim \pi R_M^c$  with  $J_M^c\lambda_{ab} \sim cH_{c1}^c/4\pi$  ( $H_{c1}^c/H_{c1}^{ab} = \gamma$ ). These assumptions lead to the integrated Meissner current

$$I_M \sim \left( \frac{c}{4\pi} \right) \pi (R_M^{ab} H_{c1}^{ab} + R_M^c H_{c1}^c) \\ \sim 8.5 R_M^c H_{c1}^c = 0.035 \text{ A}, \quad (11)$$

and the extra current  $I_M - \pi R_M^{ab} R_M^c J_c = 0.015 \text{ A}$ . The anisotropic model reduces the total current by 40%, but the vertical dimension of the Meissner hole becomes more acceptable.

An alternative explanation for the anomalously large induction step is that in a superconductor under the self-field, a large in-plane component of the critical current density  $J_c^{ab}$  could flow at the top and bottom regions of the Meissner cylinder, where the vortices are essentially bent to the in-plane direction (see Fig. 9). The contribution to the induction due to  $J_c^{ab}$  in this region is demonstrated with a numerical simulation in Ref. [41]. Therefore, to re-estimate the extra current, we need to substitute the originally assumed  $J_c^c$  which induces  $c$ -direction induction with  $J_c^{ab}$  that induces an in-plane one. The net current is then enhanced by  $\sim S(J_c^{ab} - J_c^c)$ . Here  $S$  is the smearing area of the in-plane vortices (yellow area in Fig. 9), and the superscripts on  $J_c$  indicate their induction



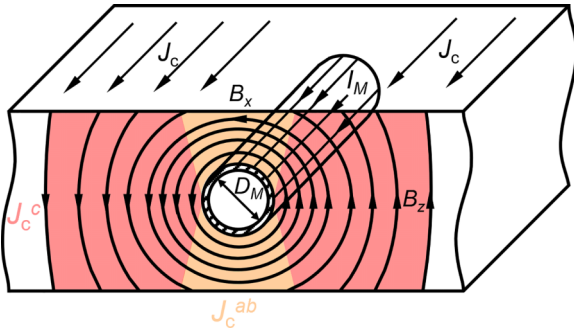


FIG. 9. Schematics of the critical current and vortex distribution in the vicinity of a Meissner hole. The hatched area indicates the skin thickness of the cylinder. Red and yellow regions represent areas where  $J_c^c$  and  $J_c^{ab}$  are dominant, respectively.

orientation. In  $\text{YBa}_2\text{Cu}_3\text{O}_7$ , a remarkably anisotropic pinning force leads to  $J_c^{ab}/J_c^c \sim 5$  [42]. In that case, the net current could be further multiplied, as simulated in Ref. [3]. However, we failed to find such a large contrast between  $J_c^{ab}$  and  $J_c^c$  in  $(\text{Ba}_{0.33}\text{Rb}_{0.67})\text{Fe}_2\text{As}_2$  (see Supplemental Material [20]). Similar to other 122-type IBSs like  $\text{Ba}(\text{Fe}_{0.93}\text{Co}_{0.07})_2\text{As}_2$  and  $(\text{Ba}_{0.6}\text{K}_{0.4})\text{Fe}_2\text{As}_2$ , the anisotropy of  $J_c$  is not pronounced in this system ( $J_c^{ab}/J_c^c \sim 1$ ) [20,28]. To solve the above paradox, we may need to imagine an oversized Meissner hole that somehow defies the restriction of minimal  $R_M$  given by the pinning-tension balance, which, however, keeps the size implied by the width of the induction steps,  $\sim 15 \mu\text{m}$ , in Fig. 4(d). Such a colossal Meissner hole, taking the elliptical proportion derived above (which does not break the sample thickness limitation unlike the case of the circle), should bear an extra current of  $0.015 \text{ A} \times (15 \mu\text{m}/2 \mu\text{m})^2 \sim 1 \text{ A}$ . Figure 10 shows the simulation of an induction step generated by such an extra portion of current flowing in our superconducting sample. Notice that this is merely a schematic representation and does not capture certain realistic physical aspects, such as the flux density distribution resulting from the current flow at the surface. The result reproduces the experimental observation under the same situation. However, it is also noteworthy that in estimating the extra current in the colossal Meissner hole, we implicitly assumed that the skin thickness is proportional to the size of the Meissner hole.

#### IV. SUMMARY

We reported the Meissner hole observed in a new 122-type IBS  $(\text{Ba}_{0.33}\text{Rb}_{0.67})\text{Fe}_2\text{As}_2$ . Compared to the flux front for virgin penetration of vortices, the interface between vortices and

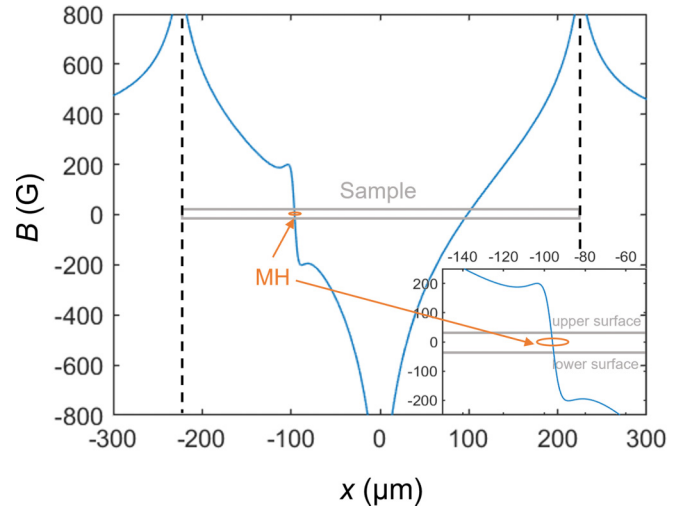


FIG. 10.  $B_z(x)$  profile simulation of a 1 A extra current flowing along  $y$  direction inside a superconducting sample (gray rectangle) at  $B_z(x) = 0$  given by Eq. (2), under an external field  $H = 300 \text{ Oe}$ . The orange ellipse reflects the relative position and size of the assumed anisotropic colossal Meissner hole.

antivortices upon remagnetization has a distinct meandering structure, called the “Meissner hole,” accompanied by a locally doubled current. We tentatively modeled the dynamics of the Meissner hole based on the relaxation of homogeneous current and built a relationship between the normalized creep rate of the Meissner hole and the normalized relaxation rate of magnetization, which qualitatively explains the obtained experimental data. The quantitative discrepancy between experiments and theory is attributed to the complicated electrodynamics of the Meissner current, which accelerates the local motion of the current segments. While it is yet difficult to properly model the geometric effect of the Meissner hole based on microscopic vortex dynamics, we provided strong evidence to claim that the configurational feature of the Meissner hole could effectively accelerate the vortex relaxation at low fields. In the end, a simple model calculation clarifies the necessity of bringing anisotropic superconductivity into the discussion for the quantitative understanding of features related to the Meissner hole.

#### ACKNOWLEDGMENT

This work was partly supported by a Grant in Aid for Scientific Research (A) (Grant No. 17H01141) from the Japan Society for the Promotion of Science (JSPS).

- [1] E. H. Brandt, Geometric barrier and current string in type-II superconductors obtained from continuum electrodynamics, *Phys. Rev. B* **59**, 3369 (1999).
- [2] M. V. Indenbom, T. Schuster, H. Kuhn, H. Kronmüller, T. W. Li, and A. A. Menovsky, Observation of current strings in  $\text{Bi}_2\text{Sr}_2\text{CaCu}_2\text{O}_8$  single crystals, *Phys. Rev. B* **51**, 15484 (1995).

- [3] V. K. Vlasko-Vlasov, U. Welp, G. W. Crabtree, D. Gunter, V. I. Kabanov, and V. I. Nikitenko, Meissner holes in superconductors, *Phys. Rev. B* **56**, 5622 (1997).
- [4] L. M. Fisher, P. E. Goa, M. Baziljevich, T. H. Johansen, A. L. Rakhmanov, and V. A. Yampol'skii, Hydrodynamic instability of the flux-antiflux interface in type-II superconductors, *Phys. Rev. Lett.* **87**, 247005 (2001).

- [5] L. M. Fisher, A. Bobyl, T. H. Johansen, A. L. Rakhmanov, V. A. Yampol'skii, A. V. Bondarenko, and M. A. Obolenskii, Anisotropic origin of the bending instability of the flux-antiflux interface in type-II superconductors, *Phys. Rev. Lett.* **92**, 037002 (2004).
- [6] C. Baggio, M. Howard, and W. van Saarloos, Dynamics and stability of vortex-antivortex fronts in type-II superconductors, *Phys. Rev. E* **70**, 026209 (2004).
- [7] E. E. Dvash, I. Shapiro, B. Rosenstein, N. Logoboy, and B. Y. Shapiro, Vortex-antivortex annihilation and flux turbulence in layered type-II superconductors, *J. Low Temp. Phys.* **167**, 39 (2012).
- [8] F. Bass, B. Y. Shapiro, I. Shapiro, and M. Shvartsner, Flux-antiflux interface in type-II superconductors, *Phys. Rev. B* **58**, 2878 (1998).
- [9] L. Landau and E. Lifshitz (eds.), *Fluid Mechanics*, 2nd ed., (Elsevier, Amsterdam, 1987), Chap. III, pp. 95–156.
- [10] H. Koppe, The current carrying capacity of a hard superconducting wire in zero external field, *Phys. Status Solidi B* **17**, K229 (1966).
- [11] J. E. A. M. Campbell, *Critical Currents in Superconductors* (Taylor & Francis, London, 1973).
- [12] V. K. Vlasko-Vlasov, U. Welp, G. W. Crabtree, D. Gunter, V. V. Kabanov, V. I. Nikitenko, and L. M. Paulius, Meissner holes and turbulent structures in superconductors in unidirectional and rotating fields, *Phys. Rev. B* **58**, 3446 (1998).
- [13] T. Frello, M. Baziljevich, T. H. Johansen, N. H. Andersen, T. Wolf, and M. R. Koblischka, Flux turbulence in  $\text{NdBa}_2\text{Cu}_3\text{O}_{6+x}$  and underdoped  $\text{YBa}_2\text{Cu}_3\text{O}_{6+x}$  single crystals, *Phys. Rev. B* **59**, R6639 (1999).
- [14] I. F. Voloshin, A. V. Kalinov, L. M. Fisher, V. A. Yampol'skii, A. Bobyl, and T. H. Johansen, Development of macroturbulent instability in a YBCO single crystal, *Low Temp. Phys.* **35**, 627 (2009).
- [15] M. R. Koblischka, T. H. Johansen, M. Baziljevich, H. Hauglin, H. Bratsberg, and B. Y. Shapiro, Turbulent relaxation in the vortex lattice, *Europhys. Lett.* **41**, 419 (1998).
- [16] T. H. Johansen, M. Baziljevich, D. V. Shantsev, P. E. Goa, Y. M. G. perin, W. N. Kang, H. J. Kim, E. M. Choi, M. S. Kim, and S. I. Lee, Dendritic magnetic instability in superconducting  $\text{MgB}_2$  films, *Europhys. Lett.* **59**, 599 (2002).
- [17] S. Mohan, Y. Tsuchiya, Y. Nakajima, and T. Tamegai, Instability of vortex-antivortex interface in optimally doped  $\text{Ba}(\text{Fe}_{1-x}\text{Co}_x)_2\text{As}_2$ , *Phys. Rev. B* **84**, 180504(R) (2011).
- [18] S. Aswartham, M. Abdel-Hafiez, D. Bombor, M. Kumar, A. U. B. Wolter, C. Hess, D. V. Evtushinsky, V. B. Zabolotnyy, A. A. Kordyuk, T. K. Kim, S. V. Borisenko, G. Behr, B. Büchner, and S. Wurmehl, Hole doping in  $\text{BaFe}_2\text{As}_2$ : The case of  $\text{Ba}_{1-x}\text{Na}_x\text{Fe}_2\text{As}_2$  single crystals, *Phys. Rev. B* **85**, 224520 (2012).
- [19] T. Taen, F. Ohtake, S. Pyon, T. Tamegai, and H. Kitamura, Critical current density and vortex dynamics in pristine and proton-irradiated  $\text{Ba}_{0.6}\text{K}_{0.4}\text{Fe}_2\text{As}_2$ , *Supercond. Sci. Technol.* **28**, 085003 (2015).
- [20] See Supplemental Material at <http://link.aps.org/supplemental/10.1103/PhysRevB.109.224504> for the  $M$ - $T$ ,  $M$ - $H$ , and  $J_c$ - $H$  of the single crystal used in MO, the masked sample used in proton-irradiation, and evaluation of the anisotropic  $J_c$ . The Supplemental Material also contains  $J_c$  anisotropy data for  $(\text{Ba}_{0.6}\text{K}_{0.4})\text{Fe}_2\text{As}_2$  and some figures taken from Ref. [43].
- [21] P. W. Anderson, Theory of flux creep in hard superconductors, *Phys. Rev. Lett.* **9**, 309 (1962).
- [22] A. Soibel, E. Zeldov, M. Rappaport, Y. Myasoedov, T. Tamegai, S. Ooi, M. Konczykowski, and V. B. Geshkenbein, Imaging the vortex-lattice melting process in the presence of disorder, *Nature (London)* **406**, 282 (2000).
- [23] M. Yasugaki, K. Itaka, M. Tokunaga, N. Kameda, and T. Tamegai, Magneto-optical observations of crossing-lattice state in  $\text{Bi}_2\text{Sr}_2\text{CaCu}_2\text{O}_{8+y}$ , *Phys. Rev. B* **65**, 212502 (2002).
- [24] T. Ren, S. Pyon, and T. Tamegai, Growth and characterizations of iron-based superconductor  $(\text{Ba}_{1-x}\text{Rb}_x)\text{Fe}_2\text{As}_2$  single crystals, *J. Phys.: Conf. Ser.* **1975**, 012013 (2021).
- [25] M. V. Feigel'man, V. B. Geshkenbein, A. I. Larkin, and V. M. Vinokur, Theory of collective flux creep, *Phys. Rev. Lett.* **63**, 2303 (1989).
- [26] M. Feigel'man, V. Geshkenbein, and A. Larkin, Pinning and creep in layered superconductors, *Physica C (Amsterdam, Neth.)* **167**, 177 (1990).
- [27] G. Blatter, M. V. Feigel'man, V. B. Geshkenbein, A. I. Larkin, and V. M. Vinokur, Vortices in high-temperature superconductors, *Rev. Mod. Phys.* **66**, 1125 (1994).
- [28] T. Tamegai, T. Taen, H. Yagyuda, Y. Tsuchiya, S. Mohan, T. Taniguchi, Y. Nakajima, S. Okayasu, M. Sasase, H. Kitamura, T. Murakami, T. Kambara, and Y. Kanai, Effects of particle irradiations on vortex states in iron-based superconductors, *Supercond. Sci. Technol.* **25**, 084008 (2012).
- [29] R. Willa, A. E. Koshelev, I. A. Sadovskyy, and A. Glatz, Strong-pinning regimes by spherical inclusions in anisotropic type-II superconductors, *Supercond. Sci. Technol.* **31**, 014001 (2018).
- [30] Y. Nakajima, Y. Tsuchiya, T. Taen, T. Tamegai, S. Okayasu, and M. Sasase, Enhancement of critical current density in Co-doped  $\text{BaFe}_2\text{As}_2$  with columnar defects introduced by heavy-ion irradiation, *Phys. Rev. B* **80**, 012510 (2009).
- [31] A. Gurevich, Electromagnetic instabilities and current structures in anisotropic superconductors, *Phys. Rev. B* **46**, 3638 (1992).
- [32] C. P. Bean, Magnetization of hard superconductors, *Phys. Rev. Lett.* **8**, 250 (1962).
- [33] C. P. Bean, Magnetization of high-field superconductors, *Rev. Mod. Phys.* **36**, 31 (1964).
- [34] Y. Yeshurun, A. Malozemoff, and A. Shaulov, Magnetic relaxation in high-temperature superconductors, *Rev. Mod. Phys.* **68**, 911 (1996).
- [35] T. Taen, Y. Nakajima, T. Tamegai, and H. Kitamura, Enhancement of critical current density and vortex activation energy in proton-irradiated Co-doped  $\text{BaFe}_2\text{As}_2$ , *Phys. Rev. B* **86**, 094527 (2012).
- [36] G. Li, W. Z. Hu, J. Dong, Z. Li, P. Zheng, G. F. Chen, J. L. Luo, and N. L. Wang, Probing the superconducting energy gap from infrared spectroscopy on a  $\text{Ba}_{0.6}\text{K}_{0.4}\text{Fe}_2\text{As}_2$  single crystal with  $T_c = 37$  K, *Phys. Rev. Lett.* **101**, 107004 (2008).
- [37] R. Flükiger, Overview of superconductivity and challenges in applications, *Rev. Accel. Sci. Technol.* **05**, 1 (2012).
- [38] A. Sudbø, E. H. Brandt, and D. A. Huse, Multiple coexisting orientations of flux lines in superconductors with uniaxial anisotropy, *Phys. Rev. Lett.* **71**, 1451 (1993).
- [39] N. Ni, S. L. Bud'ko, A. Kreyssig, S. Nandi, G. E. Rustan, A. I. Goldman, S. Gupta, J. D. Corbett, A. Kracher, and P. C. Canfield, Anisotropic thermodynamic and transport properties



- of single-crystalline  $\text{Ba}_{1-x}\text{K}_x\text{Fe}_2\text{As}_2$  ( $x = 0$  and  $0.45$ ), [Phys. Rev. B \*\*78\*\*, 014507 \(2008\)](#).
- [40] C. Martin, R. T. Gordon, M. A. Tanatar, H. Kim, N. Ni, S. L. Bud'ko, P. C. Canfield, H. Luo, H. H. Wen, Z. Wang, A. B. Vorontsov, V. G. Kogan, and R. Prozorov, Nonexponential london penetration depth of external magnetic fields in superconducting  $\text{Ba}_{1-x}\text{K}_x\text{Fe}_2\text{As}_2$  single crystals, [Phys. Rev. B \*\*80\*\*, 020501\(R\) \(2009\)](#).
- [41] L. W. Conner, A. P. Malozemoff, and I. A. Campbell, Self-fields and critical-current-density anisotropy of high-temperature superconductors, [Phys. Rev. B \*\*44\*\*, 403 \(1991\)](#).
- [42] L. Civale, B. Maiorov, A. Serquis, J. O. Willis, J. Y. Coulter, H. Wang, P. N. Jia, Q. X. amd Arendt, M. Jaime, J. L. MacManus-Driscoll, M. P. Maley, and S. R. Foltyn, Understanding high critical currents in  $\text{YBa}_2\text{Cu}_3\text{O}_7$  thin films and coated conductors, [J. Low Temp. Phys. \*\*135\*\*, 87 \(2004\)](#).
- [43] S. Pyon, A. Takahashi, I. Veshchunov, T. Tamegai, S. Ishida, A. Iyo, H. Eisaki, M. Imai, H. Abe, T. Terashima, and A. Ichinose, Large and significantly anisotropic critical current density induced by planar defects in  $\text{CaKFe}_4\text{As}_4$  single crystals, [Phys. Rev. B \*\*99\*\*, 104506 \(2019\)](#).